Biophysical Journal
Article

Biophysical Society

Cell and Tissue Scale Forces Coregulate *Fgfr2*-Dependent Tetrads and Rosettes in the Mouse Embryo

Jun Wen,[1,2] Hirotaka Tao,[2] Kimberly Lau,[2] Haijiao Liu,[1,3] Craig A. Simmons,[1,3] Yu Sun,[1,*] and Sevan Hopyan[2,4,5,*]
[1]Department of Mechanical and Industrial Engineering, University of Toronto, Toronto, Ontario, Canada; [2]Program in Developmental and Stem Cell Biology, Research Institute, The Hospital for Sick Children, Toronto, Ontario, Canada; [3]Institute of Biomaterials and Biomedical Engineering and [4]Department of Molecular Genetics, University of Toronto, Toronto, Ontario, Canada; and [5]Division of Orthopaedic Surgery, Hospital for Sick Children and University of Toronto, Toronto, Ontario, Canada

ABSTRACT What motivates animal cells to intercalate is a longstanding question that is fundamental to morphogenesis. A basic mode of cell rearrangement involves dynamic multicellular structures called tetrads and rosettes. The contribution of cell-intrinsic and tissue-scale forces to the formation and resolution of these structures remains unclear, especially in vertebrates. Here, we show that *Fgfr2* regulates both the formation and resolution of tetrads and rosettes in the mouse embryo, possibly in part by spatially restricting atypical protein kinase C, a negative regulator of non-muscle myosin IIB. We employ micropipette aspiration to show that anisotropic tension is sufficient to rescue the resolution, but not the formation, of tetrads and rosettes in *Fgfr2* mutant limb-bud ectoderm. The findings underscore the importance of cell contractility and tissue stress to multicellular vertex formation and resolution, respectively.

INTRODUCTION

Epithelial sheets remodel during development due to cell divisions, cell-shape changes, and cell rearrangements (1–4). An important remodeling mechanism in animals is cell intercalation, in which a limited variety of rearrangements account for a substantial amount of tissue remodeling. Cell divisions and cell-neighbor exchange events are sometimes not concurrent among invertebrates (5), though cell divisions commonly precipitate cell rearrangements in vertebrates (4,6,7). Two of the most common types of rearrangement involve multicellular structures among four (tetrads, – T1 exchange) (1) or more (rosettes) (2) cells. Formation of these structures requires actomyosin contraction of selective cell interfaces to form a transient central vertex in both *Drosophila* (1,2,8) and mouse (9,10), and it is driven upstream by molecular cues that impart spatial information, such as the anteroposterior embryo axis in *Drosophila* (11,12). Subsequent resolution of a multicellular vertex may alter the local landscape, and directionally biased resolution of multiples of these processes can morph tissue on a larger scale.

Various morphogenetic cell behaviors are oriented by a combination of cell-intrinsic and cell-extrinsic forces (7,13–21). There is evidence in mouse and *Drosophila* that tissue tension is planar polarized (18,22) and orients the resolution axis of multicellular vertices (7,13,15). In *Drosophila*, laser ablation experiments have distinguished between 1) local stresses attributable to cell-intrinsic myosin II contractions, which shrink junctions to form tetrads and rosettes and also promote new junction formation during resolution of those structures, and 2) cell-extrinsic tissue-scale stress, which orients the axes of new junctions (2,13,23). In mouse limb-bud ectoderm, local and tissue scale forces become parallel as the early mouse limb bud emerges from the flank such that multicellular vertices form and resolve along the same axis. A combination of mesodermal growth and ectodermal convergence at the dorsoventral midline of the emerging limb bud generates tension in the plane of the ectoderm. That tension is initially dorsoventrally biased at limb initiation and becomes proximodistally oriented as the bud emerges (7). Tissue tension is *required* to orient multicellular vertex resolution along the axis of growth, but it remains unclear whether tension is *sufficient* to promote or to orient the resolution axes of multicellular vertices.

The resolution of multicellular vertices and the formation of new cell interfaces along the axis of growth

Submitted August 8, 2016, and accepted for publication April 17, 2017.
*Correspondence: sun@mie.utoronto.ca or sevan.hopyan@sickkids.ca
Editor: Alexander Dunn.
http://dx.doi.org/10.1016/j.bpj.2017.04.024

requires Pten (24), medial myosin (13), Toll receptors (11), and regulated myosin II phosphorylation (15,25) in *Drosophila*. In mouse mutants, molecular control of multicellular vertex resolution has been obscured by pleiotropic effects. *Fgfr2* is an important regulator of ectodermal remodeling in the mouse embryo and is essential for growth of the early limb bud (7,26,27). However, it is unclear whether the primary problem in *Fgfr2* mutants is lack of anisotropic tissue tension or inability to remodel cell-cell junctions. Here, we employ loss- and gain-of-function approaches to show that *Fgfr2* promotes cell interface oscillation, which is required for the formation and resolution of tetrads and rosettes. Tissue tension is sufficient to resolve, but not to form, multicellular vertices in mouse ectoderm.

MATERIALS AND METHODS

Mouse lines

Analysis was performed using the mouse strains CAG::myr-Venus (28), mTmG (Jackson Laboratory, *Gt(ROSA)26Sortm4(ACTB_tdTomato,_EGFP)Luo/J*), *R26R:Venus-Actin* (29), floxed *Fgfr2* (30), and ectoderm-specific *Crect* (31). To generate mutant embryos, *flox/flox* females carrying the appropriate fluorescent reporter were bred to *flox/+;Cre* males. Both *mTmG* and *Crect* were employed in a heterozygous fashion. For all experiments, wild-type (WT) embryos were designated as WT, and $Fgfr2^{fl/+}$*;Crect;mTmG* embryos were designated as *Fgfr2* mutants. All animal experiments were performed in accordance with protocols approved by the Hospital for Sick Children Animal Care Committee.

Live imaging

Embryos were submerged just below the surface in 50% rat serum in Dulbecco's modified Eagle's medium (Invitrogen, Carlsbad, CA) in a 35 mm dish with a central coverglass that was surrounded by 4% agarose at 37°C in 5% CO_2 (7,32). Embryos were immobilized using pulled glass needles to pin the head and tail to the agarose and position the initiating limb bud directly against the coverglass. A Quorum Information Technologies (Calgary, Alberta, Canada) spinning-disk confocal microscope at 10× or 20× magnification was used to acquire time-lapse images at 5 min intervals for periods of up to 3 h. GFP fluorophores were excited using a 488 nm argon laser. Confocal images were acquired as *z*-stacks of *xy* images in 2- to 5-μm steps. Raw data were processed using Volocity 6.3, then imported into Image J for further analysis.

Quantification of cell behaviors

Cell outlines in confocal images were automatically identified using a plugin in Image J (Automated Multicellular Tissue Analysis) developed by the Advanced Digital Microscopy Core Facility at the Institute for Research in Biomedicine (Barcelona, Spain). After ectodermal cells were segmented in the confocal image sequences for each time point, several cell behaviors were quantified, including the cell elongation axis, cell-division orientation, cell-rearrangement polarity, and cortical actin oscillation. Angles measured from 0° to 179° with respect to the line of reference (which was plotted as 0°) were grouped into bins of 30° and represented in polar plots symmetrically about the horizontal axis. Angles ranging from 0° to 179° were also shown as positive acute angles (0°–90°) to represent the extent of alignment with the line of reference. Acute angles were grouped into five bins of 18° and were represented in histograms. The line of reference was the dorsoventral (DV) limb-bud axis unless otherwise specified. The following describes specifically how each type of cell behavior was measured.

The outline of each cell was fitted into an ellipse, and the longitudinal and transverse axes were calculated automatically in Image J. The angles between each longitudinal axis of the fitted cell ellipses and the line of reference were calculated and referred to as the cell elongation angle. Metaphase-to-telophase transition orientation was defined by a line connecting the centroid of the two daughter cells. The angles between the metaphase-to-telophase transition orientation and the line of reference were measured and referred to as the cell division angle. Multicellular tetrads and rosettes were identified manually in confocal time-lapse sequences. When the central apex of the multicellular structure resolved and vanished, the rearrangement polarity was measured as the angle between the longitudinal axis of the ellipse outlined by each tetrad or rosette and the line of reference.

Oscillation of cortical actin contraction was quantified by manually measuring the length of cell interfaces labeled by Venus-actin in each frame. Interface lengths were normalized against their initial lengths in the first frame of image sequences. Normalized rates of change of interfacial lengths were plotted over time. The amplitude of the oscillations was measured using the standard deviation of the interfacial length for each interface over time. Oscillation of cell interfaces along DV and anteroposterior (AP) axes was analyzed separately to test the possibility of oscillation anisotropy.

Immunofluorescence

Embryonic-day (E) 9.5–10.5 mouse embryos were fixed overnight in 4% paraformaldehyde in phosphate-buffered saline (PBS) followed by three washes in PBS. Embryos were permeabilized in 0.1% Triton X-100 in PBS for 20 min and blocked in 5% normal donkey serum (in 0.05% Triton X-100 in PBS) for 1 h. Embryos were incubated in primary antibody for 5 h at room temperature, followed by incubation overnight at 4°C. Embryos were washed in 0.05% Triton X-100 in PBS (three washes of 15 min each) and then incubated in secondary antibody for 1 h at room temperature in the dark. Images were acquired using a Quorum Information Technologies spinning-disk confocal microscope, and image analysis was performed using Volocity software and Image J.

The antibodies used were atypical protein kinase C (aPKC) (sc-216, Santa Cruz, rabbit, 1:100), Zo 1 (Invitrogen 40–2200, rabbit, 1:200), nonmuscle myosin IIB (MYOIIB) (Covance PRB-445P, rabbit, 1:500), and Frizzled 6 (AF1526, R&D Systems, goat, 1:250). All secondary antibodies were purchased from Jackson Immunoresearch and used at 1:1000 dilution.

Atomic force microscopy

The apparent Young's moduli of early limb-bud ectodermal cells were examined using a commercial atomic force microscope (AFM) (BioScope Catalyst, Bruker, Billerica, MA) under an inverted microscope (Eclipse-Ti, Nikon, Tokyo, Japan). Young's modulus was incorporated into a finite-element model (FEM) as a material property and was also interpreted as a proxy for the ectodermal cell cortical tension. The detailed experimental approach and data analysis methods follow protocols regarding the use of a colloidal probe, described elsewhere (33). Briefly, colloidal-force probes were custom made by attaching a borosilicate glass microsphere (10 μm diameter; Sigma-Aldrich, St. Louis, MO) to an AFM cantilever (MLCT-D, Bruker/Veeco) using epoxy glue. Force-distance curves were acquired at distal, middle, and proximal regions of limb-bud ectoderm using a consistent 200 pN contact force at an indentation rate of 1 Hz. Because the contact force was relatively small, minimum substratum influence of the underlying mesoderm was assumed, and therefore, no explicit sample thickness correction was performed. At each location of the limb bud, five force curves were acquired with a minimum wait time of 15 s between successive measurements to minimize any history effect (34).

To calculate Young's modulus from force-distance curves, the Hertz model with Sneddon's modification was used (35). Young's modulus was calculated using the following equation for spherical probes:

$$F = \left(\frac{4}{3}\right)\sqrt{R}\left[\frac{E}{1-\nu^2}\right]h^{3/2},$$

where F is the loading force, R is the probe radius, E is the Young's modulus, ν is Poisson's ratio, and h is the indentation depth.

The spring constant of AFM cantilevers was calibrated for each experiment using the thermal noise fluctuation method (36). Embryos were immobilized against a 4% agarose gel pad by pulled glass needles in 50% rat serum/50% Dulbecco's modified Eagle's medium. AFM measurements were performed within 30 min. of dissection.

Optical projection tomography and limb-bud morphology analysis

E9.5 mouse embryos were harvested and fixed in 4% paraformaldehyde overnight at 4°C. The optical projection tomography (OPT) system was custom built and is fully described elsewhere (37). Three-dimensional (3D) data sets were reconstructed from auto-fluorescence projection images acquired over a 10 min scan time at an isotropic voxel size of 3.85 μm. The 3D surface renderings of OPT data were generated by Amira software, version 5.3.3 (VSGG, Burlington, MA).

Finite-element modeling

FEM was employed to investigate force/stress propagation and deformation of the limb-bud ectodermal sheet under different mechanical forces. All simulations were implemented in ANSYS v14.0 (ANSYS, Canonsburg, PA). 3D models of the ectodermal layer were created according to optical projection tomography images of the limb bud at the 18-somite stage. The length, width, and thickness of the ectodermal layer in the FEM models was 1445 μm (AP axis), 212 μm (DV axis), and 10 μm (proximodistal axis), respectively. The bulging region at the center of the sheet was modeled to be 30 μm tall to resemble the shape of the limb bud.

The mechanical behavior of the ectodermal sheet was modeled as a continuum with homogeneous viscoelastic material properties rather than as individual cells. A generalized Kelvin model (38) was used to account for the tissue viscoelastic behavior. An instantaneous elastic modulus of 0.085 kPa was assigned to limb-bud ectodermal tissue based on AFM indentation data (7). Viscous relaxation of the ectodermal modulus was calculated based on limb-bud compression relaxation data reported previously (38) and was implemented in ANSYS as two-pair Prony relaxation with relative moduli of 0.1 and 0.4 and relaxation time constants of 8 and 45 s, respectively. A Poisson's ratio of 0.4 was used, as is common for biological material (39).

Micropipette aspiration pressure was modeled as negative pressure exerted on a precise area on the dorsal ectoderm where the micropipette contacted the ectoderm. Boundary conditions were applied to the ectodermal sheet model in which all six degrees of freedom were fixed. A frictionless support underneath the ectodermal sheet was added to resemble the mesodermal support normal to the ectoderm while allowing tangential displacement within the plane.

Ten-node tetrahedral elements were used to discretize all geometries in our model. Since stress and deformation are linearly proportional to the exact applied load, the qualitative characteristics of the stress pattern on the limb bud, such as the direction and ratio of the principal stresses, would be the same at different load magnitudes. Viscoelastic properties according to compression data only represent passive tissue properties, without taking into account the long-term viscous behavior presumably caused by dynamic cell rearrangements or tissue fluidity (40).

Micropipette aspiration

The micropipette aspiration system consists of a confocal microscope with a motorized XY translation stage, a micromanipulator (MX7600, Siskiyou, Yreka, CA) for micropipette positioning, and a custom-built pressure system with a differential pressure transducer (PX409-10WDWU5V, Omega Engineering, Stanford, CT). In experiments, a 35°-bevelled micropipette with an inner diameter of 35 μm was mounted on the micromanipulator and connected to the vacuum pressure system (Fig. S1 *C*). The embryo was placed down on its flank, immobilized on the petri dish, and imaged with a confocal microscope (Fig. 2 *A*). The following subtasks were subsequently performed: 1) the system automatically detected the micropipette and moved it to the vicinity of the limb bud (Fig. S2 *A*); 2) the system detected tissue-micropipette contact before negative pressure was applied (Fig. S2 *B*); and 3) the system compensated for the 3D drift trajectory of the limb-bud tissue to maintain stable tissue-micropipette contact during the 2 h experimental periods (Fig. S2 *C*). Micropipette position and aspiration pressure were controlled cooperatively using visual feedback and pressure sensor feedback (Fig. S2, *D* and *E*).

RESULTS

DV-oriented cell behaviors normally shape the ectoderm of the early mouse limb bud (7). (The DV axis of lateral plate ectoderm becomes gradually oriented along the predominant proximodistal axis of growth as the limb bud emerges.) To examine cell behaviors in the absence of a conditional *Fgfr2* allele (30), we employed an ectoderm-specific Cre recombinase, *Crect* (31), together with a transgenic cell membrane reporter (*mT/mG*) (41). In the limb field of 18- to 22-somite-stage *Fgfr2$^{f/f}$;Crect;mT/mG* mouse embryos, ectodermal cells exhibited loss of DV-oriented elongation and division planes, as observed during time-lapse imaging of intact embryos (Fig. 1, *A–G*; Fig. S1 *A*). The total number of multicellular vertices per unit area was diminished in the *Fgfr2* mutant ectoderm (Fig. 1 *H*; Fig. S1 *B*), as was the frequency of multicellular vertex resolution during 3 h imaging sessions (Fig. 1 *I*; Fig. S1, *C* and *D*). Moreover, the usual DV resolution axis of tetrads and rosettes was disoriented in the *Fgfr2* mutant ectoderm. Despite proper formation of a transient central vertex, mutant ectodermal rosettes formed (7) and resolved along the AP embryo axis (Fig. 1, *J* and *K*; Fig. S1, *E*; Movies S1 and S2). Therefore, *Fgfr2* is required to promote the formation and DV resolution of multicellular vertices. Two cellular processes potentially can explain these observations: *Fgfr2* promotes contractility and/or junctional remodeling (13,15).

Since tissue tension is a key driver of new junction formation (7,13,15), we examined this parameter in *Fgfr2* mutants. Given that cells exhibit a positive Poisson ratio (39), their apical surface area should increase when tensed along one axis, as is apparent during AP germband extension due to an AP pulling force (surface area decrease is expected when cells are compressed) (18). In the limb-bud ectoderm, we found that the apical surface areas of WT cells where DV stress predominates (7) were larger than those of non-limb lateral plate cells. In contrast, the apical surfaces of

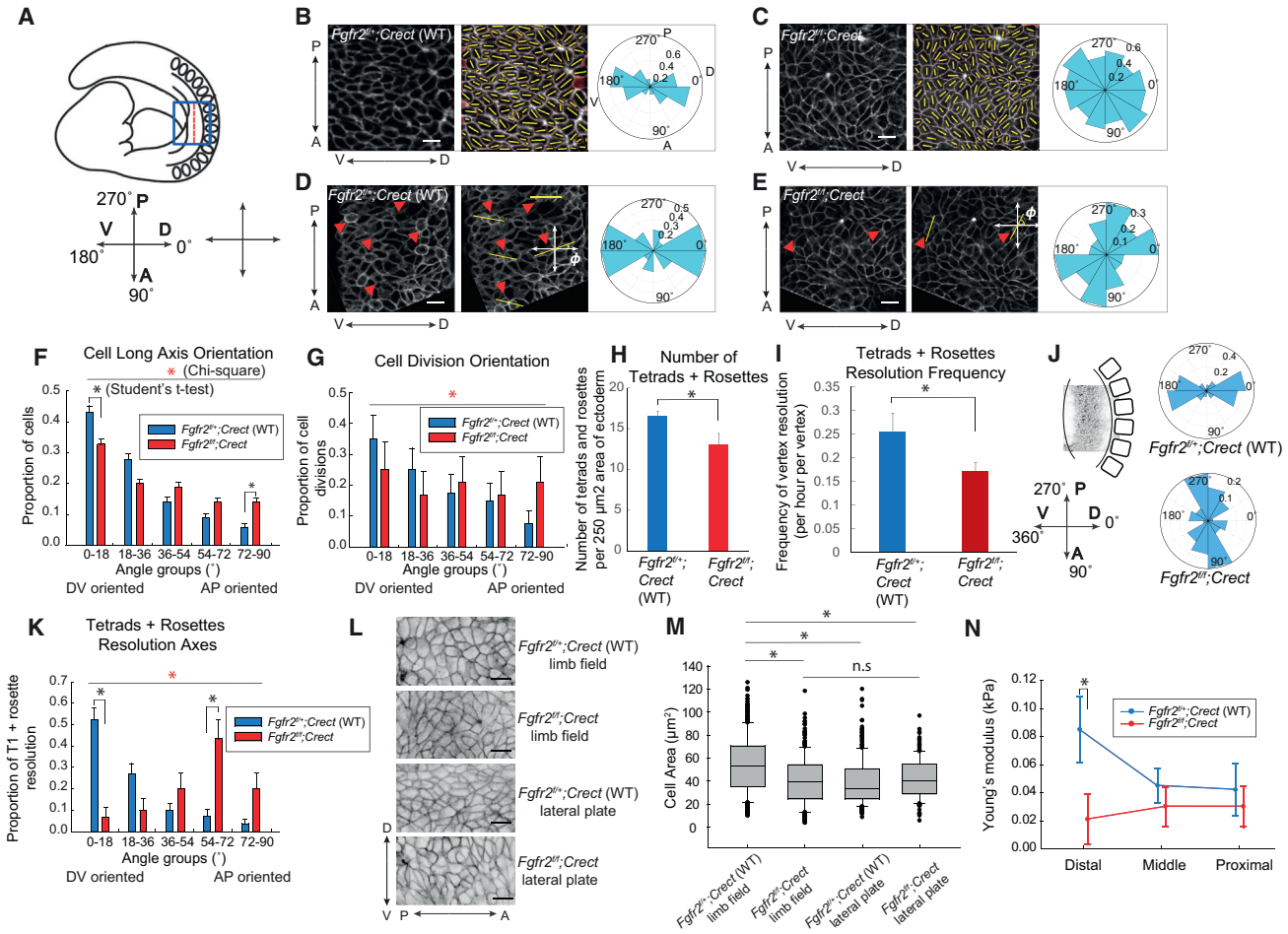

FIGURE 1 DV-oriented ectodermal cell behaviors and tension are diminished in conditional *Fgfr2* mutants. (*A*) Schematic depiction of the position of a mouse forelimb bud that grows distally out of the plane of the page. The blue box indicates the region of interest for analysis. (*B* and *C*) Left: Confocal section of pre-AER (20 som) WT (*B*) and conditional *Fgfr2* mutant (*C*) limb field ectoderm. Centre: Segmented cells with yellow bars showing cell long axes. Right: Polar plots representing orientation of long axis angles of limb-bud ectodermal cells ($n = 3$ WT embryos, 150 cells, and 3 *Fgfr2* mutant embryos, 160 cells). (*D* and *E*) Confocal sections of WT (*D*) and conditional *Fgfr2* mutant (*E*) limb field ectoderm. Red triangles indicate dividing cells and yellow bars indicate cell division axes. Polar plots represent cell division angles. (*F*) Distributions of cell long axes with the DV and AP axes represented by 0° and 90°, respectively ($n = 5$ embryos per condition; 569 cells were examined for the WT versus 699 cells for the *Fgfr2* mutant). Distribution was significantly different ($p < 0.0001$, chi-square test (*red asterisk*); for the WT versus mutant 0–18° bin, $p = 0.0002$, Student's *t*-test (*black asterisk*); for the WT versus mutant 72–90° bin, $p < 0.0001$, Student's *t*-test (*black asterisk*)). (*G*) Distribution of cell division angles ($n = 5$ embryos per condition; WT-40 divisions examined versus *Fgfr2* mutant-24 divisions examined) was significantly different ($p = 0.00014$, chi-square test). (*H*) The total number of tetrads and rosettes per a 250 μm^2 area of ectoderm ($n = 5$ WT, $n = 4$ *Fgfr2* mutant 18- to 22-somite embryos, $p = 0.03$ by Student's *t*-test). (*I*) Frequency of tetrad and rosette resolution per multicellular vertex in WT and *Fgfr2* mutants ($n = 5$ 18- to 22-somite embryos per condition, $p = 0.0491$, Student's *t*-test). (*J*) Polar plots represent the resolution axes of tetrads and rosettes in WT and conditional *Fgfr2* mutant embryos during 2–3 h time-lapse sessions. (*K*) Distribution of resolution angles among resolving tetrads and rosettes in WT and conditional *Fgfr2* mutant limb-bud ectoderm with respect to the DV axis ($n = 5$ 18- to 22-somite embryos per condition, with 82 tetrads and rosettes examined for the WT embryos versus 30 tetrads and rosettes for the *Fgfr2* mutant. Distribution was significantly different ($p < 0.0001$, chi-square test; WT versus mutant for the 0–18° bin, $p < 0.0001$, Student's *t*-test; WT versus mutant for the 54–72° bin, $p = 0.0006$, Student's *t*-test). (*L*) Confocal section of the apical surface of the WT limb field, the *Fgfr2* mutant limb field, the WT lateral plate, and the *Fgfr2* mutant lateral plate ectoderm. (*M*) Box plots demonstrate the distribution of ectodermal cell surface area in the WT limb field (300 cells examined), the *Fgfr2* mutant limb field (270 cells examined), the WT lateral plate (274 cells examined), and the *Fgfr2* mutant lateral plate (154 cells examined). The average apical cell area in the WT limb field was significantly larger than in the *Fgfr2* mutant limb field ($p = 0.00423$, Student's *t*-test), the WT lateral plate ($p = 0.00033$, Student's *t*-test), and the *Fgfr2* mutant lateral plate ($p < 0.005$ by Student's *t*-test). The average cell area was not significantly different between the WT lateral plate ectoderm and the *Fgfr2* mutant limb field ectoderm ($p = 0.612$ by Student's *t*-test), between the WT lateral plate ectoderm and the *Fgfr2* mutant lateral plate ectoderm ($p = 0.146$ by Student's *t*-test), and between the *Fgfr2* mutant limb field ectoderm and the *Fgfr2* mutant lateral plate ectoderm ($p = 0.34$ by Student's *t*-test). (*N*) AFM measured the apparent Young's moduli of the proximal, middle, and distal regions of the WT and conditional *Fgfr2* mutant limb buds ($n = 5$ 18- to 22-somite embryos per condition; distal WT versus mutant, $p = 0.0204$, Student's *t*-test). Scale bars represent 10 μm (*B–E* and *K*). Error bars indicate the SEM.

Fgfr2$^{f/f}$*;Crect* mutant ectodermal cells in the limb field were similar to those in the non-limb lateral plate and smaller than those in the WT limb field (Fig. 1, *L* and *M*), suggesting that stress was diminished in mutant limb-bud ectoderm. To measure the distribution of stress in live embryonic tissue, we conducted AFM measurements (7,42). *Fgfr2*$^{f/f}$*;Crect* mutants lacked a stress gradient that emanates from the prospective apical ectodermal ridge at the distal end of the limb bud (7) (Fig. 1 *N*). Therefore, loss of a stress differential correlates with diminished frequency and disorientation of cell rearrangements in *Fgfr2* mutants.

To test whether anisotropic tissue stress is sufficient to promote new junction formation, we artificially restored an anisotropic stress field in mutants by micropipette aspiration of the ectoderm. In brief, we developed a custom micropipette aspiration system to exert precisely calibrated and stable tension to the ectodermal sheet of intact embryos in situ for an extended period during live confocal imaging (Fig. 2, *A* and *B*). The micropipette aspiration system incorporates optical and pressure sensor feedback to enable control of the micropipette position and applied aspiration pressure (see Materials and Methods, Fig. S2). An FEM that incorporated the actual geometry of the 18-somite limb field was built to simulate the ectodermal stress field (Fig. 2 *C*). Aspiration-induced force was modeled as negative pressure acting on the area covered by the micropipette aperture that was used in experiments (inner diameter, 35 μm). Simulated aspiration at a range of pressures created

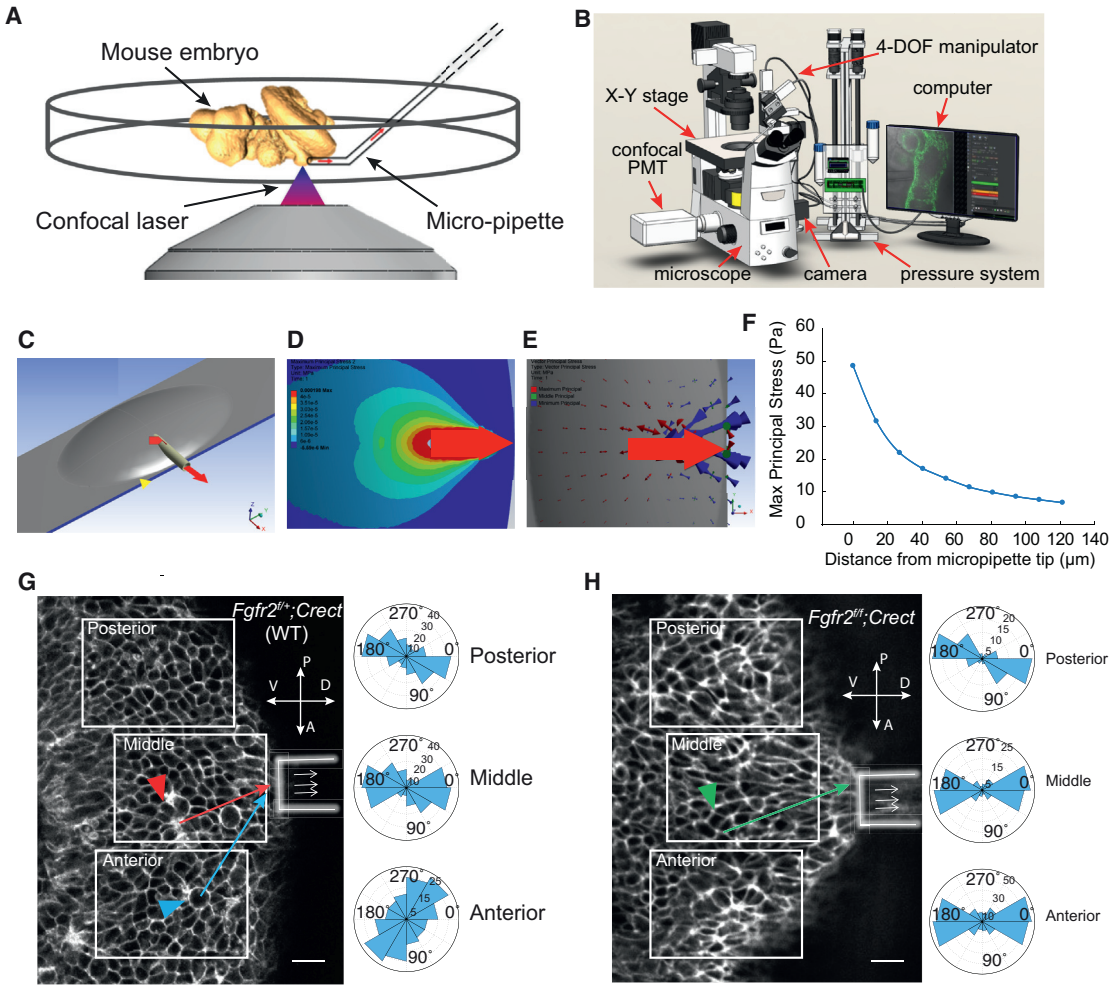

FIGURE 2 Micropipette aspiration of mouse embryonic ectoderm. (*A*) Schematic of simultaneous micropipette aspiration and confocal scanning of a mouse embryonic limb bud. (*B*) The system consists of a micropipette mounted on a micromanipulator, a motorized XY stage, a confocal microscope, a CMOS camera, and a host computer. Pressure was controlled by precisely positioning two water reservoirs. (*C*) Finite-element simulation of micropipette aspiration. (*D*) Stress field due to micropipette aspiration. (*E*) Simulated maximal principal stresses (*red arrows*) were oriented toward the micropipette opening. (*F*) Given 0.1 nN/μm^2 of aspiration pressure, the graph represents the simulated magnitude of maximal principal stress versus distance from the micropipette opening. (*G* and *H*) Micropipette aspiration of limb-bud ectoderm in WT (*Fgfr2*$^{f/+}$*;Crect*) and mutant (*Fgfr2*$^{f/f}$*;Crect*) embryos. Three polar plots represent the cell elongation angles of ectodermal cells corresponding to each of the three white-boxed regions. Tissue was pulled to the aperture, but no cells were lost into the pipette. Red, blue, and green arrowheads identify a rosette, dividing cell and tetrad, respectively, which are shown in further detail in Fig. 3 *D*. The corresponding arrows indicate the direction of applied tissue force. Scale bars represent 10 μm (*G* and *H*).

a radial stress field with a magnitude that decreased away from the micropipette aperture and was directionally biased toward it (Fig. 2, *D* and *E*). We determined that with an applied pressure of 0.1 nN/μm^2, stress would dissipate from 50 to 10 Pa over a distance of 100 μm from the micropipette aperature (Fig. 2 *F*). Accordingly, each ectodermal cell would therefore experience 5–10 nN of force, which has been shown by others to be sufficient to elongate cells, recruit myosin, and induce transcription (23,43,44).

We applied a constant aspiration pressure of 0.1 nN/μm^2 to the limb field of intact 18-somite embryos for 2 h periods and simultaneously performed live, confocal imaging. Within several seconds of initiating aspiration, ectodermal cells in both WT and *Fgfr2$^{f/f}$;Crect* mutants became elongated. Cell shapes were changed up to 10 cell diameters away from the micropipette aperture and were oriented in a radial fashion that corresponded to the new stress field (Fig. 2, *G* and *H*). Therefore, as expected, tension instantaneously reoriented longitudinal cell axes.

To evaluate tetrad and rosette rearrangements, we first compared WT embryos with or without aspiration using the DV axis as a reference. The native DV orientation of cell rearrangements was significantly diminished by microsuction (Fig. 3 *A*), suggesting that cells were responding to the ectopic stress field by rotating obliquely toward it at a range of angles, as shown in Fig. 2 *G*. Micropipette aspiration did not increase the total number of tetrads and rosettes (Fig. 3 *B*) despite cell stretching (Fig. 2, *G* and *H*). Also, the time to resolution of tetrads and rosettes under native (WT, unaspirated) conditions was similar to that under aspiration conditions (in WT and *Fgfr2* mutant backgrounds) (Fig. S3 *A*). Together, these findings suggest that cell elongation and new interface formation are distinct processes. However, aspiration did increase the resolution frequency of existing vertices in *Fgfr2$^{f/f}$;Crect* mutants to WT levels (Fig. 3 *C*). An ectopic stress field is therefore insufficient to promote the formation of multicellular vertices but does restore their resolution frequency.

To precisely quantify how the axes of cell divisions and cell rearrangements respond to extrinsic stress, we employed a new reference axis connecting each target cell to the micropipette aperture. Cell division (ϕ1), T1 (ϕ2), and rosette resolution angles (ϕ3) were measured with respect to this reference axis (Fig. 3 *D*). The distributions of angle ϕ1 indicated that mutant ectodermal daughter cells were no longer statistically different from those of WT cells (Fig. 3 *E*), implying that they responded to ectopic stress. However, this effect on mutant cell division was no longer apparent when orientation was categorized as aligned versus misaligned (Fig. S3 *B*), suggesting that reorientation of cell division may require a higher stress threshold. The resolution axes of tetrads and rosettes became aligned with the imposed axis of stress. Interestingly, this alignment held true to a similar extent for *Fgfr2$^{f/f}$;Crect* mutants and WT embryos (Fig. 3, *F–H*; Fig. S3 C; Movies 3 and 4). These results indicate that ectopic tissue tension is sufficient to reorient multicellular axis resolution in conditional *Fgfr2* mutant embryos. They imply that junctional remodeling is intact but force generation is compromised in the absence of *Fgfr2*.

To test whether *Fgfr2* regulates force generation, we examined the oscillatory nature of cell interface length changes that are due to actomyosin contractions and are required for new junction formation (13,15). The rate of change of cell interface lengths was measured in vivo during live imaging experiments. As expected based on the anisotropic stress pattern (7), WT limb-bud ectodermal cells exhibited greater interface length rate of change and amplitude along the DV axis (parallel to AP interface) compared to the AP axis (parallel to DV interface). In contrast, *Fgfr2* mutant cells exhibited isotropic rate of change and amplitude (Fig. 4, *A–C*). Therefore, *Fgfr2* is required to promote anisotropic cell interface oscillation that is a consequence of cytoskeletal contraction (but is not necessarily linearly related to the degree of contraction).

To examine how *Fgfr2* regulates this process, we studied the distribution of cytoskeletal and cell polarity proteins. We previously showed that planar polarity of cortical actin was diminished in *Fgfr2* mutants, although MYOIIB was not polarized (7), nor were select markers of cell polarity FZD6 and ZO1 (Fig. S4). However, quantification revealed that the MyoIIB immunostain intensity was diminished in *Fgfr2* mutants (Fig. 4, *D–F*). Interestingly, we also observed mislocalization of aPKC, which is best known as a component of the Par complex that regulates apicobasal cell polarity. This protein also links apicobasal polarity to planar cell behavior, in part by contributing to the formation and localization of adherens junctions and to the attachment of cortical actomyosin to the cell membrane (45–48). aPKC was predominantly located at the apical domain of WT ectodermal cells, as expected. In *Fgfr2* mutant ectoderm, however, the aPKC expression domain was expanded basolaterally (Fig. 4, *G–J*). These findings suggest that *Fgfr2* promotes MYOIIB-dependent cell interface oscillation and regulates some components of cell polarity.

DISCUSSION

The importance of active versus passive mechanisms of cell intercalation has long been a focus of inquiry. An early computational model of epithelial remodeling assumed that junctional rearrangements accommodate the balance of forces at cell contact sites. Interestingly, stress relaxation in the absence of active junctional remodeling or active cell interdigitation was sufficient to account for cell rearrangements that are observed during *Fundulus* epiboly (17). Experimentalists deconstructed the phenomenon of widespread cell intercalation to basic units of rearrangement involving tetrads and rosettes (1,2). These approaches prompted separate consideration of the formation and resolution stages of

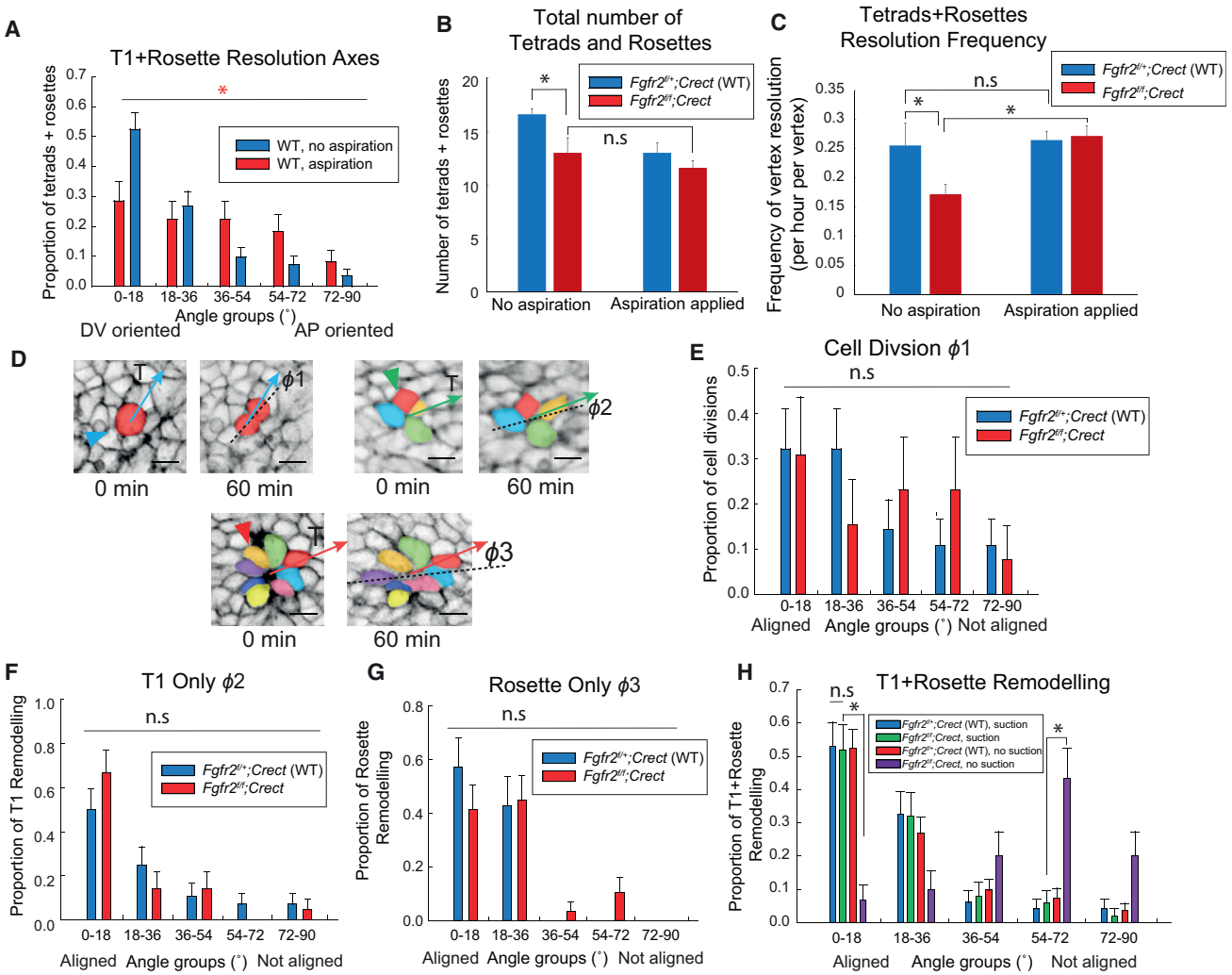

FIGURE 3 Ectopic tension reorients cell rearrangements. (*A*) Comparative distribution of resolution axes for WT tetrads and rosettes with or without aspiration with respect to the native DV axis ($n = 5$ 18–22 som. embryos per condition; $p = 0.0167$, chi-square test). (*B*) The total number of *Fgfr2* mutant tetrads and rosettes per 250 μm^2 area of ectoderm was not increased by aspiration ($n = 5$ WT, $n = 4$ *Fgfr2* mutant 18- to 22-somite embryos, $p = 0.37$ by Student's *t*-test). (*C*) The frequency of tetrad and rosette resolution per vertex was rescued in *Fgfr2* mutants ($n = 5$ 18- to 22-somite embryos per condition; mutant before aspiration versus mutant after aspiration, $p = 0.0355$, Student's *t*-test; WT before aspiration versus mutant after aspiration, $p = 0.3368$. (*D*) Time series demonstrating 20-somite limb-bud ectodermal cell division, T1 (tetrad), and rosette resolutions. The cell division angle, $\phi 1$, T1 resolution angle, $\phi 2$, and rosette resolution angle, $\phi 3$, were defined with respect to the direction of externally applied tension, as indicated by the arrows. (*E*) Distribution of cell division angles, $\phi 1$, with respect to the axis of ectopic stress in WT and *Fgfr2* mutant limb-bud ectoderm ($n = 5$ 18- to 22-somite embryos per condition) was not significantly different ($p = 0.6723$ by the chi-square test). (*F*) Distribution of tetrad resolution angles, $\phi 2$, with respect to the axis of ectopic stress. ($n = 5$ 18- to 22-somite embryos per condition, with 28 tetrads examined in the WT and 21 tetrads examined in mutants; $p = 0.5588$, chi-square test). (*G*) Distribution of rosette resolution angles, $\phi 3$, with respect to the axis of ectopic stress ($n = 5$ 18- to 22-somite embryos per condition, with 21 rosettes examined in the WT and 29 rosettes examined in mutants; $p = 0.3159$, chi-square test). (*H*) Distribution of resolution angles for tetrads and rosettes combined ($\phi 2$ and $\phi 3$) in WT and *Fgfr2* mutants after aspiration was not significantly different ($n = 5$ 18- to 22-somite embryos per condition; 49 tetrads and rosettes examined in WT, and 50 tetrads and rosettes were examined in mutants; $p = 0.9554$, chi-square test). The resolution axes of mutant tetrads and rosettes were aligned with ectopic stress induced by aspiration (for the 0–18° bin, $p < 0.0001$; for the 54–72° bin, $p = 0.0004$, by Student's *t*-test). Scale bars in (*D*) represent 10 μm. Error bars indicate SEM.

these multicellular structures, and recent evidence has underscored the importance of cell-extrinsic tissue stress as a spatial cue that orients resolution (7,13,15,18,22). The data in this study support a model in which *Fgfr2* promotes cortical oscillation through MYOIIB, rather than junctional remodeling, to induce the formation of multicellular vertices. FGF signaling is also required to promote MYOIIB-dependent apical constriction that induces rosette-shaped proneuromast formation in the lateral line of zebrafish (49–52), suggesting that there is a degree of conservation in the morphogenetic role of FGF.

Ectopic tissue tension was sufficient to reorient the resolution, but not rescue the formation, of tetrads and rosettes in *Fgfr2* mutants. Our observation that tension can overcome

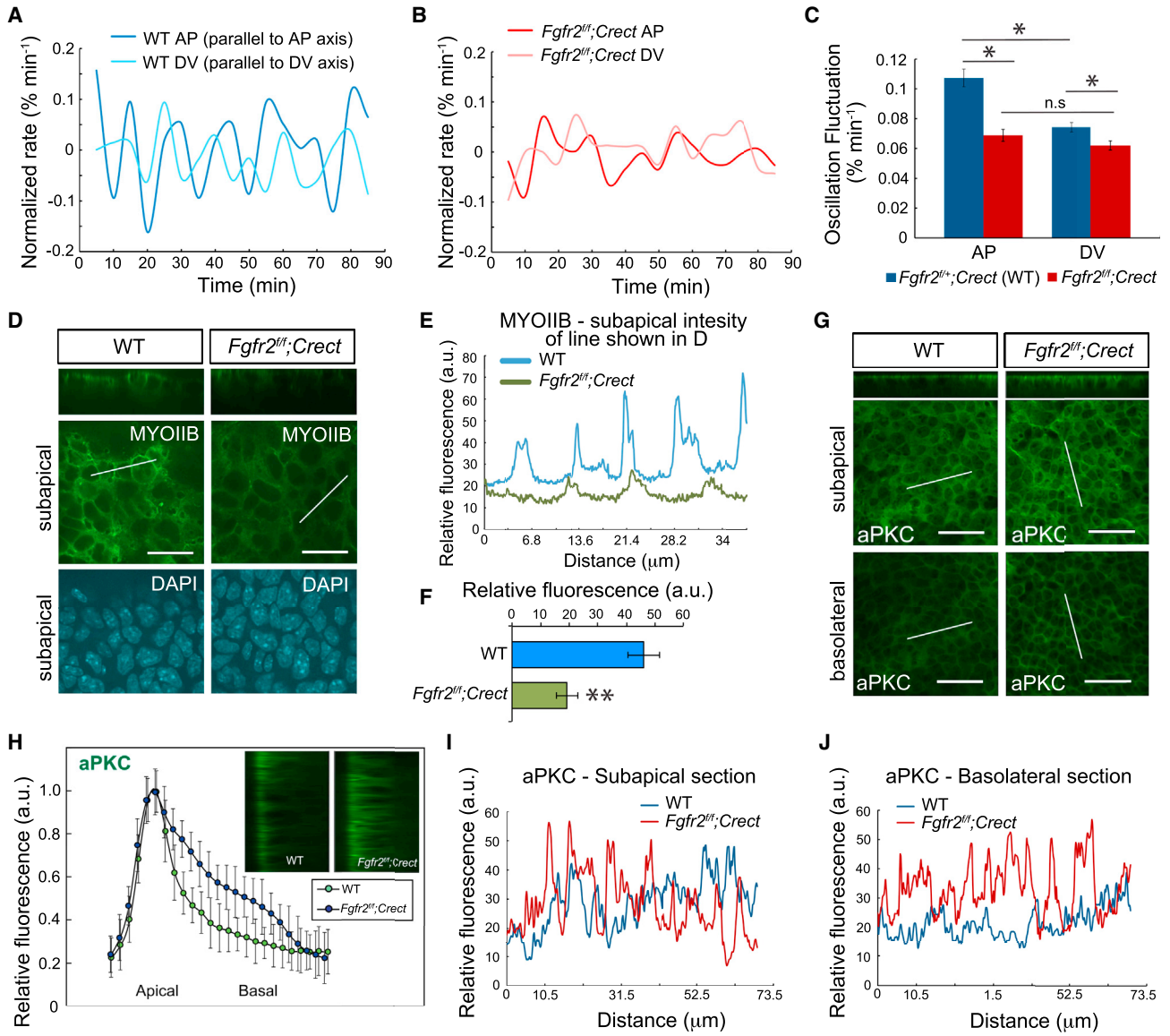

FIGURE 4 *Fgfr2* regulates anisotropic cell interface oscillation. (*A* and *B*) Rate of change of interface length from time-lapse videos of WT (*Fgfr2*$^{f/+}$; *Crect*) (*A*) and conditional *Fgfr2* mutant (*B*) limb-bud ectoderm, normalized to the initial interface length. Shown are representative curves for AP and DV interfaces (parallel to DV and AP axes, respectively). (*C*) Oscillation amplitude of AP and DV interfaces in WT and conditional *Fgfr2* mutant limb-bud ectoderm ($n = 40$ interfaces for each condition; WT AP versus DV interfaces, $p < 0.001$; mutant AP versus DV interfaces, $p = 0.1807$; WT AP interfaces versus mutant AP interfaces, $p < 0.001$; WT DV interfaces versus mutant DV interfaces, $p = 0.0071$, Student's *t*-test). (*D*) *xy* sections at the DV boundary of 21-somite WT and conditional *Fgfr2* mutant limb-bud ectoderm showing MYOIIB (*green*) and DAPI (*blue*). (*E*) Fluorescence intensity profiles of subapical MYOIIB in WT and conditional *Fgfr2* mutant ectoderm corresponding to the oblique white lines shown on the en-face images in (*D*). (*F*) Overall relative fluorescence of three separate 40× subapical fields of view in each of three 20- to 22-somite embryos ($p < 0.001$). (*G*) *xy* sections at the DV boundary of 20-somite WT and conditional *Fgfr2* mutant limb-bud ectoderm showing aPKC. Shown are *z*-sections (*top*) and subapical and basolateral sections of the same region. (*H*) Quantification of aPKC intensity from the apical to the basal aspect of WT and conditional *Fgfr2* mutant ectoderm. Inset: *xz* sections showing lateral views of ectoderm with the apical aspect on the left. Intensities were normalized to the maximal level at the apical surface for each condition ($n = 3$ separate 40× fields in each of three 20- to 22-somite embryos). (*I* and *J*) Comparison of aPKC fluorescence intensity at the subapical (*I*) and basolateral (*J*) levels of WT and *Fgfr2* mutant ectoderm, represented as intensity profiles of the oblique white lines shown on the corresponding en-face images in (*G*). Scale bars represent 25 μm (*D*) and 50 μm (*G*). Error bars indicate the mean ± SE.

partially depleted MYOIIB in *Fgfr2* mutants to resolve multicellular vertices underscores the importance of cell-extrinsic mechanical regulation of polarized cell behaviors. The data imply that formation of tetrads and rosettes requires cell-intrinsic MYOIIB, and we speculate that this is due to greater energy requirement relative to the resolution stage.

Antecorrelation between aPKC and MYOIIB is consistent with the role of aPKC as a kinase that negatively regulates MYOIIB directly (53) and indirectly through

Rho-associated kinase (54,55) and dampens pulsatile actomyosin contractions (46,56). The basolateral expansion of aPKC seen here is reminiscent of spatial redistribution of this protein during mitosis in *Drosophila*, which aids assembly of a relatively isotropic metaphase cortex (57). Whether and how basolateral expansion of aPKC actually diminishes subapical MYOIIB in limb-bud ectoderm is not addressed by this study although one possibility is that recruitment of MYOIIB is affected in this context by global cellular levels of aPKC indirectly through Rho-associated kinase. Nonetheless the FGF pathway, a recognized regulator of growth and cell fate, also regulates motor and polarity proteins implying that morphogenesis and pattern formation are closely coordinated.

Mechanisms that form and resolve multicellular vertices may be intertwined. Both actin and myosin accumulate in response to tension (23,58,59), and their coordinated contractions likely change the local tensile landscape that feeds back to orient resolution angles. Evidence for a co-dependent relationship includes our observation that cell oscillation is associated with vertex resolution and is reminiscent of the requirement for medial myosin contraction during new junction formation in *Drosophila* (13,15). Multicellular vertex formation and resolution often take place at different angles, so it remains unclear how tissue forces might help to coordinate the orientation of these events. Quantitative evaluation of all morphogenetic events that shape a given tissue (60,61) together (60,61) with a detailed understanding of how cells sense force cues and translate that information into spatially appropriate junctional rearrangements (62) are steps in the right direction.

SUPPORTING MATERIAL

Four figures and four movies are available at http://www.biophysj.org/biophysj/supplemental/S0006-3495(17)30440-X.

AUTHOR CONTRIBUTIONS

J.W., Y.S., and S.H. designed the experiments and wrote the manuscript. J.W., K.L., H.T., and H.L. performed experimental work. J.W., H.T., H.L., and C.A.S. performed theoretical and image analyses.

ACKNOWLEDGMENTS

We thank Rodrigo Fernandez-Gonzalez for critical evaluation of the manuscript. This study was supported by the Canadian Institutes of Health Research, MOP 126115 (S.H.), and by a Canada Research Chair in Micro and Nano Engineering Systems (Y.S.).

REFERENCES

1. Bertet, C., L. Sulak, and T. Lecuit. 2004. Myosin-dependent junction remodelling controls planar cell intercalation and axis elongation. *Nature*. 429:667–671.
2. Blankenship, J. T., S. T. Backovic, …, J. A. Zallen. 2006. Multicellular rosette formation links planar cell polarity to tissue morphogenesis. *Dev. Cell.* 11:459–470.
3. Irvine, K. D., and E. Wieschaus. 1994. Cell intercalation during *Drosophila* germband extension and its regulation by pair-rule segmentation genes. *Development.* 120:827–841.
4. Keller, R. E. 1978. Time-lapse cinemicrographic anaIysis of superficiaI ceII behavior during and prior to gastrulation in X*enopus laevis*. *J. Morphol.* 157:223–248.
5. Gibson, M. C., A. B. Patel, …, N. Perrimon. 2006. The emergence of geometric order in proliferating metazoan epithelia. *Nature*. 442:1038–1041.
6. Firmino, J., D. Rocancourt, …, J. Gros. 2016. Cell division drives epithelial cell rearrangements during gastrulation in chick. *Dev. Cell.* 36:249–261.
7. Lau, K., H. Tao, …, S. Hopyan. 2015. Anisotropic stress orients remodelling of mammalian limb bud ectoderm. *Nat. Cell Biol.* 17:569–579.
8. Rauzi, M., P. F. Lenne, and T. Lecuit. 2010. Planar polarized actomyosin contractile flows control epithelial junction remodelling. *Nature*. 468:1110–1114.
9. Lienkamp, S. S., K. Liu, …, G. Walz. 2012. Vertebrate kidney tubules elongate using a planar cell polarity-dependent, rosette-based mechanism of convergent extension. *Nat. Genet.* 44:1382–1387.
10. Williams, M., W. Yen, …, A. Sutherland. 2014. Distinct apical and basolateral mechanisms drive planar cell polarity-dependent convergent extension of the mouse neural plate. *Dev. Cell.* 29:34–46.
11. Paré, A. C., A. Vichas, …, J. A. Zallen. 2014. A positional Toll receptor code directs convergent extension in *Drosophila*. *Nature*. 515:523–527.
12. Zallen, J. A., and E. Wieschaus. 2004. Patterned gene expression directs bipolar planar polarity in *Drosophila*. *Dev. Cell.* 6:343–355.
13. Collinet, C., M. Rauzi, …, T. Lecuit. 2015. Local and tissue-scale forces drive oriented junction growth during tissue extension. *Nat. Cell Biol.* 17:1247–1258.
14. Legoff, L., H. Rouault, and T. Lecuit. 2013. A global pattern of mechanical stress polarizes cell divisions and cell shape in the growing *Drosophila* wing disc. *Development.* 140:4051–4059.
15. Yu, J. C., and R. Fernandez-Gonzalez. 2016. Local mechanical forces promote polarized junctional assembly and axis elongation in *Drosophila*. *eLife.* 5:e10757.
16. Aigouy, B., R. Farhadifar, …, S. Eaton. 2010. Cell flow reorients the axis of planar polarity in the wing epithelium of *Drosophila*. *Cell.* 142:773–786.
17. Weliky, M., and G. Oster. 1990. The mechanical basis of cell rearrangement. I. Epithelial morphogenesis during *Fundulus* epiboly. *Development.* 109:373–386.
18. Butler, L. C., G. B. Blanchard, …, B. Sanson. 2009. Cell shape changes indicate a role for extrinsic tensile forces in *Drosophila* germ-band extension. *Nat. Cell Biol.* 11:859–864.
19. Bosveld, F., I. Bonnet, …, Y. Bellaïche. 2012. Mechanical control of morphogenesis by fat/dachsous/four-jointed planar cell polarity pathway. *Science.* 336:724–727.
20. Luxenburg, C., E. Heller, …, E. Fuchs. 2015. Wdr1-mediated cell shape dynamics and cortical tension are essential for epidermal planar cell polarity. *Nat. Cell Biol.* 17:592–604.
21. Gibson, W. T., J. H. Veldhuis, …, M. C. Gibson. 2011. Control of the mitotic cleavage plane by local epithelial topology. *Cell.* 144:427–438.
22. Lye, C. M., G. B. Blanchard, …, B. Sanson. 2015. Mechanical coupling between endoderm invagination and axis extension in *Drosophila*. *PLoS Biol.* 13:e1002292.
23. Fernandez-Gonzalez, R., Sde. M. Simoes, …, J. A. Zallen. 2009. Myosin II dynamics are regulated by tension in intercalating cells. *Dev. Cell.* 17:736–743.
24. Bardet, P. L., B. Guirao, …, Y. Bellaïche. 2013. PTEN controls junction lengthening and stability during cell rearrangement in epithelial tissue. *Dev. Cell.* 25:534–546.

25. Kasza, K. E., D. L. Farrell, and J. A. Zallen. 2014. Spatiotemporal control of epithelial remodeling by regulated myosin phosphorylation. *Proc. Natl. Acad. Sci. USA.* 111:11732–11737.

26. Gorivodsky, M., and P. Lonai. 2002. 4 Fgfr2/b is required for the morphogenic migration of the limb bud ectoderm. *J. Anat.* 201:418.

27. Xu, X., M. Weinstein, …, C. Deng. 1998. Fibroblast growth factor receptor 2 (FGFR2)-mediated reciprocal regulation loop between FGF8 and FGF10 is essential for limb induction. *Development.* 125:753–765.

28. Rhee, J. M., M. K. Pirity, …, A. K. Hadjantonakis. 2006. In vivo imaging and differential localization of lipid-modified GFP-variant fusions in embryonic stem cells and mice. *Genesis.* 44:202–218.

29. Abe, T., H. Kiyonari, …, T. Fujimori. 2011. Establishment of conditional reporter mouse lines at ROSA26 locus for live cell imaging. *Genesis.* 49:579–590.

30. Yu, K., J. Xu, …, D. M. Ornitz. 2003. Conditional inactivation of FGF receptor 2 reveals an essential role for FGF signaling in the regulation of osteoblast function and bone growth. *Development.* 130:3063–3074.

31. Reid, B. S., H. Yang, …, T. Williams. 2011. Ectodermal Wnt/β-catenin signaling shapes the mouse face. *Dev. Biol.* 349:261–269.

32. Wyngaarden, L. A., K. M. Vogeli, …, S. Hopyan. 2010. Oriented cell motility and division underlie early limb bud morphogenesis. *Development.* 137:2551–2558.

33. Liu, H., Y. Sun, and C. A. Simmons. 2013. Determination of local and global elastic moduli of valve interstitial cells cultured on soft substrates. *J. Biomech.* 46:1967–1971.

34. Dimitriadis, E. K., F. Horkay, …, R. S. Chadwick. 2002. Determination of elastic moduli of thin layers of soft material using the atomic force microscope. *Biophys. J.* 82:2798–2810.

35. Sneddon, I. N. 1965. The stress on the boundary of an elastic half-plane in which body forces are acting. *Proceedings of the Glasgow Mathematical Association.* 7:48–54.

36. Ohler, B. 2007. Cantilever spring constant calibration using laser Doppler vibrometry. *Rev. Sci. Instrum.* 78:063701.

37. Wong, M. D., J. Dazai, …, R. M. Henkelman. 2013. Design and implementation of a custom built optical projection tomography system. *PLoS One.* 8:e73491.

38. Forgacs, G., R. A. Foty, …, M. S. Steinberg. 1998. Viscoelastic properties of living embryonic tissues: a quantitative study. *Biophys. J.* 74:2227–2234.

39. Trickey, W. R., F. P. Baaijens, …, F. Guilak. 2006. Determination of the Poisson's ratio of the cell: recovery properties of chondrocytes after release from complete micropipette aspiration. *J. Biomech.* 39:78–87.

40. He, B., K. Doubrovinski, …, E. Wieschaus. 2014. Apical constriction drives tissue-scale hydrodynamic flow to mediate cell elongation. *Nature.* 508:392–396.

41. Muzumdar, M. D., B. Tasic, …, L. Luo. 2007. A global double-fluorescent Cre reporter mouse. *Genesis.* 45:593–605.

42. Krieg, M., Y. Arboleda-Estudillo, …, C. P. Heisenberg. 2008. Tensile forces govern germ-layer organization in zebrafish. *Nat. Cell Biol.* 10:429–436.

43. Balaban, N. Q., U. S. Schwarz, …, B. Geiger. 2001. Force and focal adhesion assembly: a close relationship studied using elastic micropatterned substrates. *Nat. Cell Biol.* 3:466–472.

44. Campàs, O., T. Mammoto, …, D. E. Ingber. 2014. Quantifying cell-generated mechanical forces within living embryonic tissues. *Nat. Methods.* 11:183–189.

45. Djiane, A., S. Yogev, and M. Mlodzik. 2005. The apical determinants aPKC and dPatj regulate Frizzled-dependent planar cell polarity in the *Drosophila* eye. *Cell.* 121:621–631.

46. Kishikawa, M., A. Suzuki, and S. Ohno. 2008. aPKC enables development of zonula adherens by antagonizing centripetal contraction of the circumferential actomyosin cables. *J. Cell Sci.* 121:2481–2492.

47. Liu, H., Z. Wu, …, L. Chen. 2013. Atypical PKC, regulated by Rho GTPases and Mek/Erk, phosphorylates Ezrin during eight-cell embryocompaction. *Dev. Biol.* 375:13–22.

48. Wang, Y. C., Z. Khan, …, E. F. Wieschaus. 2012. Differential positioning of adherens junctions is associated with initiation of epithelial folding. *Nature.* 484:390–393.

49. Ernst, S., K. Liu, …, V. Lecaudey. 2012. Shroom3 is required downstream of FGF signalling to mediate proneuromast assembly in zebrafish. *Development.* 139:4571–4581.

50. Harding, M. J., and A. V. Nechiporuk. 2012. Fgfr-Ras-MAPK signaling is required for apical constriction via apical positioning of Rho-associated kinase during mechanosensory organ formation. *Development.* 139:3130–3135.

51. Lecaudey, V., G. Cakan-Akdogan, …, D. Gilmour. 2008. Dynamic Fgf signaling couples morphogenesis and migration in the zebrafish lateral line primordium. *Development.* 135:2695–2705.

52. Nechiporuk, A., and D. W. Raible. 2008. FGF-dependent mechanosensory organ patterning in zebrafish. *Science.* 320:1774–1777.

53. Even-Faitelson, L., and S. Ravid. 2006. PAK1 and aPKCζ regulate myosin II-B phosphorylation: a novel signaling pathway regulating filament assembly. *Mol. Biol. Cell.* 17:2869–2881.

54. Ishiuchi, T., and M. Takeichi. 2011. Willin and Par3 cooperatively regulate epithelial apical constriction through aPKC-mediated ROCK phosphorylation. *Nat. Cell Biol.* 13:860–866.

55. Röper, K. 2012. Anisotropy of crumbs and aPKC drives myosin cable assembly during tube formation. *Dev. Cell.* 23:939–953.

56. David, D. J., A. Tishkina, and T. J. Harris. 2010. The PAR complex regulates pulsed actomyosin contractions during amnioserosa apical constriction in *Drosophila*. *Development.* 137:1645–1655.

57. Rosa, A., E. Vlassaks, …, B. Baum. 2015. Ect2/Pbl acts via Rho and polarity proteins to direct the assembly of an isotropic actomyosin cortex upon mitotic entry. *Dev. Cell.* 32:604–616.

58. Galkin, V. E., A. Orlova, and E. H. Egelman. 2012. Actin filaments as tension sensors. *Curr. Biol.* 22:R96–R101.

59. Pouille, P. A., P. Ahmadi, …, E. Farge. 2009. Mechanical signals trigger myosin II redistribution and mesoderm invagination in *Drosophila* embryos. *Sci. Signal.* 2:ra16.

60. Guirao, B., S. U. Rigaud, …, Y. Bellaïche. 2015. Unified quantitative characterization of epithelial tissue development. *eLife.* 4:4.

61. Etournay, R., M. Popović, …, S. Eaton. 2015. Interplay of cell dynamics and epithelial tension during morphogenesis of the *Drosophila* pupal wing. *eLife.* 4:e07090.

62. Bosveld, F., O. Markova, …, Y. Bellaïche. 2016. Epithelial tricellular junctions act as interphase cell shape sensors to orient mitosis. *Nature.* 530:495–498.